PCCP

PAPER

View Article Online
View Journal | View Issue

Check for updates

Cite this: *Phys. Chem. Chem. Phys.*, 2025, **27**, 897

DFT investigation of the impact of inner-sphere water molecules on RE nitrate binding to internal pore and external surface of MCM-22†

Tamalika Ash, *[ab] Yong Han, [ac] James W. Evans [ac] and Theresa L. Windus *[ad]

The impact of inner-sphere water molecules on the binding of rare earth (RE) nitrates to MCM-22 aluminosilicates is analyzed. We used cluster models of MCM-22 to investigate the binding phenomena through localized-basis density functional theory (DFT) calculations. We also conducted plane-wave DFT calculations for a few selected binding configurations using the entire periodic MCM-22 unit cell to check for consistency. Two different MCM-22 cluster models are developed to represent an internal pore and an external surface. Starting with pure silica MCM-22, we substituted one Si with Al and added a H atom on the O bridging the Si and Al to create a Brønsted acid site (BAS), ≡Si–{OH}–Al≡. Specifically, we investigated the binding of two RE nitrate aqua complexes, $[X(NO_3)_3(H_2O)_n]$ where n = 4 (3) for X = Nd (Yb) *via* the reaction $X(NO_3)_3(H_2O)_n$ + ≡Si–{OH}–Al≡ → ≡Si–{$OX(NO_3)_2(H_2O)_n$}–Al≡ + HNO_3 at BASs, and *via* an analogous reaction at silanol sites, ≡Si–{OH}. The above analysis just includes the inner coordination sphere H_2O. Actually, for the Nd (Yb) complex, after binding at the T1 and T2 sites (T1 site) within the internal pore, one of the H_2O molecules leaves this inner sphere. The binding strength at BASs and silanol sites is calculated from the energy change during the above reactions. One finds that Nd complexes prefer binding at the internal pore, while Yb complexes have a comparable binding preference both at the internal pore and external surface. The cluster calculations show good agreement with periodic calculations, implying that the cluster models are suitable for binding studies. Compared to the binding of non-hydrated RE nitrates, the explicit H_2O molecules have a minimal impact on overall binding energy trends, but they do increase individual binding energy values. This study also demonstrated the stronger binding affinity of BASs over silanol sites.

Received 1st September 2024,
Accepted 26th November 2024

DOI: 10.1039/d4cp03424d

rsc.li/pccp

Open Access Article. Published on 02 December 2024. Downloaded on 1/23/2026 9:32:19 PM.
This article is licensed under a Creative Commons Attribution-NonCommercial 3.0 Unported Licence.

1. Introduction

Rare-earth elements (REEs) are the set of fifteen lanthanides (La to Lu) along with chemically similar scandium (Sc) and yttrium (Y). They are recognized as critical materials because of their widespread applications in modern technologies and renewable energy solutions.[1,2] Also of concern is the potential hindrance to global economic and technological progress due to supply limitations.[3] They have numerous applications in the fields of medicine;[4–8] biology;[4–6] imaging techniques[4–6] and hi-tech industries.[9–12] Regolith-hosted ion adsorption deposits are a great source of REEs, where the REE adsorption is believed to occur *via* ionic interactions associated with dehydroxylation of surface hydroxyls.[13,14] However, the detailed binding mechanism and energetics of REEs binding on clay surfaces have been studied for only a few cases. Borst *et al.*[15] showed that the REEs are adsorbed on clays, especially on kaolinite as easily leachable 8- to 9-coordinated outer-sphere hydrated complexes. Chatterjee *et al.*[16] showed that the synthetic aluminosilicate MCM-22 can adsorb substantial amounts of Yb(III), and that the Yb(III) adsorption increases with the increase of Al-content in MCM-22. MCM-22 zeolite, an ionic clay mimic, is selected for the REE adsorption study due to the challenges in analysis for natural clay adsorbents due to defects, impurities, a mixture of phases, and local fluctuations in solution-phase conditions. Moreover, the clay mimics are well-characterized,[17–19] easy to handle under experimental conditions and tunable with respect to substitution[20] and pillaring.[21,22]

[a] *Ames National Laboratory, U.S. Department of Energy, Ames, Iowa 50011, USA. E-mail: tamalika@iastate.edu*
[b] *Department of Aerospace Engineering, Iowa State University, Ames, Iowa 50011, USA*
[c] *Department of Physics & Astronomy, Iowa State University, Ames, Iowa 50011, USA*
[d] *Department of Chemistry, Iowa State University, Ames, Iowa 50011, USA. E-mail: twindus@iastate.edu*

† Electronic supplementary information (ESI) available. See DOI: https://doi.org/10.1039/d4cp03424d

Open Access Article. Published on 02 December 2024. Downloaded on 1/23/2026 9:32:19 PM.
This article is licensed under a Creative Commons Attribution-NonCommercial 3.0 Unported Licence.

Substitutions in clay materials can play a significant role in enhancing the REE adsorption. To further elucidate the RE nitrate binding phenomena, in our recent published article,[23] we thoroughly explored the binding of $X(NO_3)_3$ (where, X = Nd, Yb) on MCM-22 zeolites employing two computational strategies: localized-basis density functional theory (DFT) and plane-wave DFT analyses. In harmony with the observation of Chatterjee *et al.*,[16] our analysis showed that the Brønsted acid sites (BASs), generated by the substitution of Si with Al, have a much stronger binding affinity towards $X(NO_3)_3$ compared to the silanol sites, establishing the important role of BASs for REE adsorption. However, in this regard, we considered $X(NO_3)_3$ complexes, where the coordination environment of the REE, *i.e.*, X, is unsaturated.

In the present study, we explore the effect of the coordination environment of the REEs on the binding phenomena. In doing so, we consider neodymium nitrate aqua, $[Nd(NO_3)_3(H_2O)_4]$ and ytterbium nitrate aqua, $[Yb(NO_3)_3(H_2O)_3]$ complexes, where four and three H_2O molecules are directly coordinated to Nd and Yb-centers forming inner-sphere complexes with a total coordination number (CN) of 10 and 9, respectively (Fig. 1). In this context, it is important to note that we focus solely on the inner-sphere REE complexes and exclude the H-bonded waters that form outer-sphere complexes.

A thorough investigation of the binding of $[X(NO_3)_3(H_2O)_n]$ complexes to MCM-22 is performed employing extensive DFT analyses. To do so, we consider two different cluster models, internal pore and external surface, to describe binding in these distinct environments. One difference between the internal pore and external surface clusters is that only BASs are present in the internal pores, whereas both BASs and silanol sites are present on the external surfaces. In Section 2.2, we explain the construction of these MCM-22 cluster models in detail. The binding of $[X(NO_3)_3(H_2O)_n]$ at BAS schematically corresponds to –

$$\equiv Si\text{–}\{OH\}\text{–}Al\equiv + [X(NO_3)_3(H_2O)_n] \rightarrow \equiv Si\text{–}\{OX(NO_3)_2(H_2O)_n\}\text{–}Al\equiv + HNO_3 \quad (1)$$

For the binding at the silanol site, a similar mechanism applies –

$$\equiv Si\text{–}\{OH\} + [X(NO_3)_3(H_2O)_n] \rightarrow \equiv Si\text{–}\{OX(NO_3)_2(H_2O)_n\} + HNO_3 \quad (2)$$

where, $\equiv Si\text{–}\{OH\}\text{–}Al\equiv$ represents the BAS motif, and $\equiv Si\text{–}\{OH\}$ represents the silanol site.

A crystalline MCM-22 unit cell has 72 tetrahedrally coordinated crystallographic Si sites, usually termed as T-sites, of which 8 are symmetrically inequivalent and traditionally labeled as T1–T8 sites.[24–28] Following our previous work,[23] here also, we consider Al substitution at T1, T2, and T3 sites in both the internal pore and external surface using the labeling scheme from ref. 24. These three T-sites are selected as they create BASs accessible to REE species in the interlayer regions. The other T-sites, from T4–T8 are embedded within the zeolite structure, and are less accessible to guest molecules.

In Section 2, we describe the development of the MCM-22 models used in our analysis, adopting the above notation for T-sites. We also describe the DFT methodology which is employed. In Section 3, we focus on presenting the results obtained from localized-basis DFT calculations using a cluster model for RE nitrate binding at BASs at an internal pore. To validate these results, we also present results from plane-wave DFT calculations in a periodic model incorporating the entire MCM-22 unit cell for RE nitrate binding at selected BASs. In this work, we prepare a larger internal pore cluster model (compared to the previous study[23] without H_2O) to explicitly account for the interactions of H_2O molecules with MCM-22 (Fig. 2). In Section 4, we summarize the results obtained for REEs binding at an external surface of MCM-22. In both cases, we compare the results obtained for binding of Nd and Yb nitrates. In Section 5, we provide a discussion in support of our findings and our conclusions.

2. MCM-22 models and DFT methodology

2.1. Consideration of RE nitrate aqua complexes

To account for the impact of explicit water molecules on the RE nitrate binding to MCM-22, the aqua complexes of RE nitrates have been considered. Neodymium nitrate is found to exist as a hexa-aqua complex in the crystal structure, with four water molecules directly attached to the metal center and two additional water molecules hydrogen bonded to the inner-sphere complexes, represented as $[Nd(NO_3)_3(H_2O)_4]\cdot 2H_2O$.[29] Similarly, ytterbium nitrate exists as penta-aqua complex with the molecular

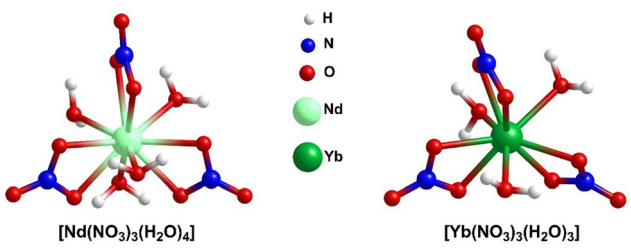

Fig. 1 Lowest energy optimized geometries for $[Nd(NO_3)_3(H_2O)_4]$ and $[Yb(NO_3)_3(H_2O)_3]$.

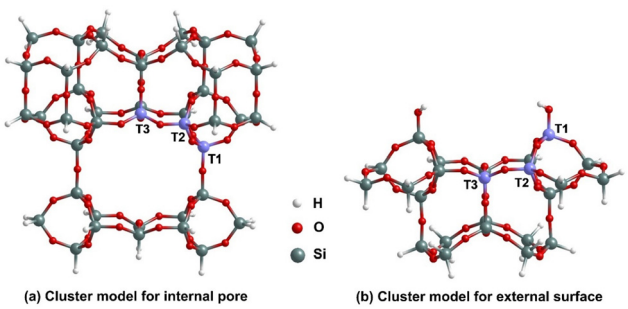

Fig. 2 Cluster models for (a) the internal pore, and (b) the external surface binding sites for RE nitrates in MCM-22 highlighting the T1, T2 and T3 sites.

 This journal is © the Owner Societies 2025

Open Access Article. Published on 02 December 2024. Downloaded on 1/23/2026 9:32:19 PM. This article is licensed under a Creative Commons Attribution-NonCommercial 3.0 Unported Licence.

formula $[Yb(NO_3)_3(H_2O)_3]\cdot 2H_2O$.[30] However, for the present study, we have focused on the inner-sphere REE complexes, as depicted in Fig. 1. Experimentally, during adsorption studies, solvent water molecules would also engage in hydrogen bonding with the inner-sphere coordination complex, extending the number of outer-sphere H_2O molecules just beyond two. In our current study, we aim to specifically examine the effect of water molecules directly coordinated to the Nd/Yb center on binding, rather than the influence of outer-sphere H_2O molecules, which are anticipated to have a small influence. For this reason, we have excluded the two outer-sphere H_2O molecules.

2.2. Construction of MCM-22 cluster models

To accurately capture the effect of the local environment of MCM-22 on the RE nitrate binding, two cluster models, named internal pore and external surface are considered. In Fig. 2, we illustrated the structures of these cluster models before any Al substitution. The internal pore cluster model includes forty-one Si atoms, while the external surface cluster model comprises twenty-four Si atoms, with molecular formulas $Si_{41}O_{77}H_{42}$ and $Si_{24}O_{38}H_{24}$, respectively. Compared to the cluster model of the internal pore used in our previous article,[23] a larger cluster is required here to more accurately account for the interaction between H_2O molecules and MCM-22 associated with $[X(NO_3)_3(H_2O)_n]$ binding at the 10-membered ring (MR) crossing windows or channels. The peripheral Si atoms are held fixed in their crystallographic positions corresponding to the crystalline MCM-22 system and are terminated with H atoms. This constraint avoids major restructuring of the cluster to an artificial configuration not representing the desired portion of MCM-22. Following earlier studies,[27,28,31,32] the Si–H bond distances are fixed to 1.47 Å, aligned along the bond direction corresponding to the next lattice oxygen in the periodic model for crystalline MCM-22. The rest of the atoms of the cluster models are fully relaxed. As with previous studies, Si at T1, T2, and T3 sites are substituted with Al for the internal pore cluster model. For the external surface cluster model, the Si at T2 and T3 sites are substituted with Al. In both cases H is added to the O atom bridging the Al with an adjacent Si to produce the complete BASs. The details of atomic coordinates are provided in the SI. Here, it is important to note that although the T1, T2, and T3 sites are positioned on the edge of the cluster models, in the periodic model for crystalline MCM-22, these sites are on the circumference of a large pore and thus have minimal interactions with the excluded parts. The key difference between the two cluster models, as shown in Fig. 2, is that the internal pore model has only BASs, while the external surface model includes both BASs and silanol sites. MCM-22 materials have been synthesized experimentally with pure silica (ITQ-1) and with Si : Al ratios from 42 : 1 to 25 : 1.[16] Thus, in all the latter cases, there is more than one Al per unit cell, but at least for higher Si : Al ratios, the BASs should not interact.

2.3. Computational details for localized-basis DFT analysis

All the electronic structure calculations for the cluster models are performed using the NWChem 7.0.2[33] quantum chemistry program. For analysis of energetics including geometry optimization, the PBE0 functional[34,35] in conjunction with the def2-svp basis set, developed by Ahlrichs and coworkers[36,37] for main group elements, and Stuttgart RSC Segmented basis set and ECP with 28 core electrons for REE,[38,39] have been used. The PBE0 functional incorporates a mix of Perdew–Burke–Ernzerhof (PBE) and Hartree–Fock exchange energy in a 3 : 1 ratio, along with the full PBE correlation energy. For REE modeling, the use of the ECP basis set reduces the calculation expense and accounts for the scalar relativistic effects. The van der Waals interactions are included by employing Grimme's dispersion (D3).[40] To ensure selected peripheral Si and H atoms remained in the correct positions, we used the 'fix atom' keyword under the 'constraints' directive during geometry optimization in NWChem. The default self-consistent field (SCF) convergence and geometry optimization criteria in NWChem have been used.

2.4. Construction of periodic MCM-22 models

The experimental synthesis of MCM-22 involves a precursor, MCM-22P, which consists of a periodic array of layers or slabs of aluminosilicate material (with a period of around 27.9 Å along the direction perpendicular to the layers), where the surfaces of each layer or slab are fully hydroxylated. MCM-22 forms during calcination by dehydroxylating these internal surfaces, resulting in the periodicity perpendicular to the layers decreasing by about 2.7 Å. Our model of MCM-22 used for analysis of RE nitrate binding at internal pores includes as the computational supercell an entire unit cell of the bulk MCM-22 material (with periodic boundary conditions). Thus, the dimensions of the computational cell are a, b = 14.5 Å in the plane of the layers, and c = 25.2 Å in the orthogonal direction. For the pure silica version of MCM-22, referred to as ITQ-1, this includes 72 Si and 144 O. We replaced one Si by Al for studies involving RE nitrate binding at BASs. For analysis of RE nitrate binding at an external surface of MCM-22, the model for the external surface is simply taken as the fully hydroxylated surface of the MCM-22P precursor, but expanding the vacuum region adjacent to this surface relative to MCM-22P. Specifically, the computational unit cell includes a single layer or slab of the precursor and a vacuum region with thickness no smaller than 20 Å along the direction orthogonal to the slab surfaces (again with periodic boundary conditions). Thus, now the dimension of the computational unit cell is increased to about 45.0 Å orthogonal to the layers.

2.5. Computational details for plane-wave DFT analysis

For the plane-wave DFT analysis, the VASP code[41] is used with the projector augmented wave potentials[42] developed by the VASP group. To include the van der Waals (vdW) interactions, we choose the optB88-vdW functional[43] in the electron–electron exchange-correlation component. Previous DFT calculations for the bulk properties of silica polymorphs, various vdW materials or biomaterials,[43–48] as well as various small molecules consisting of C, H, O and N,[49] indicate the reliability of this DFT method with the optB88-vdW functional. In this work,

Open Access Article. Published on 02 December 2024. Downloaded on 1/23/2026 9:32:19 PM. This article is licensed under a Creative Commons Attribution-NonCommercial 3.0 Unported Licence.

we use this plane-wave DFT method to compare with the localized atomic basis DFT analysis.

In our plane-wave DFT analyses for RE nitrate binding both within the bulk and at the surface of MCM-22, the computational supercells are selected as indicated in Section 2.4 with a k mesh of $2 \times 2 \times 1$.[50] In the structural optimization for single molecules,[49] HNO_3, $[Nd(NO_3)_3(H_2O)_4]$, or $[Yb(NO_3)_3(H_2O)_3]$, we use a periodic cubic box with any side length of 30.0 Å and with a k mesh of $1 \times 1 \times 1$. In all plane-wave DFT calculations, the energy cutoff is always taken to be 600 eV, and the energy convergence tolerance is taken to be less than 0.01 eV $Å^{-1}$ for the force on each atom. All atoms are fully relaxed during the structure optimization.

2.6. RE nitrate aqua complexes binding energies

Schematic representations of the binding reactions of $[X(NO_3)_3(H_2O)_n]$ binding at the BASs and silanol sites are given in eqn (1) and (2). The equations for the corresponding RE nitrate binding energies for both cluster and periodic MCM-22 models are as follows:

For binding at BASs, one has

$$BE(BAS) = E[\equiv Si\text{–}\{OX(NO_3)_2(H_2O)_n\}\text{–}Al\equiv] + E[HNO_3] - E[\equiv Si\text{–}\{OH\}\text{–}Al\equiv] - E[X(NO_3)_3(H_2O)_n] \quad (3)$$

For binding at the silanol site (for external surface), one has

$$BE(silanol) = E[\equiv Si\text{–}\{OX(NO_3)_2(H_2O)_n\}] + E[HNO_3] - E[\equiv Si\text{–}\{OH\}] - E[X(NO_3)_3(H_2O)_n] \quad (4)$$

where $E[\ldots]$ represents the total energy of the indicated species.

3. RE nitrate binding at an internal pore of MCM-22

3.1. Localized-basis DFT analysis

The binding of $[X(NO_3)_3(H_2O)_n]$ to Tj BASs within the cavity formed by –O–Si–O– linkages (see Fig. 3), which represent the 10 MR crossing window interlayer space in the periodic model, has been considered. Our previous work[23] considered the analogous RE nitrate binding process without the explicit H_2O.The BASs at the internal pore are termed bulk-Tj and after binding with $[X(NO_3)_3(H_2O)_n]$ complexes, they are referred to as bulk-Tj-X.

In Fig. 3, we have illustrated the lowest-energy optimized structures for the binding of $[Nd(NO_3)_3(H_2O)_4]$ complex at bulk-Tj BASs for the internal pore cluster model. In the case of bulk-T1-Nd, the binding of $[Nd(NO_3)_3(H_2O)_4]$ to the cluster causes one H_2O molecule to leave the inner-coordination sphere and bridge between the oxygen of an –Al–O–Si– linkage of the cluster (1.82 Å) and one of the directly bound H_2O molecules (1.55 Å) through a hydrogen bonding interaction, resulting in a total coordination number (CN) of 9 for Nd. Similarly, for bulk-T2-Nd also, the CN around Nd becomes 9 after binding, with the leaving H_2O molecule dangling between the directly bound H_2O molecule and cluster with hydrogen bonding distances of 1.61 and 1.86 Å, respectively. Unlike the previous two scenarios, for bulk-T3-Nd, the geometry around the Nd center remains unchanged before and after binding to the cluster, maintaining a 10 coordinated complex. As given in eqn (1), the binding of $[Nd(NO_3)_3(H_2O)_4]$ complex to the cluster results in the release of one molecule of nitric acid in all three cases. The structures of bulk-Tj-Nd also show that the H_2O molecules attached to the Nd center form hydrogen bonds with the oxygen of –O–Si–O– linkage of the cluster, with bond distances varying between 1.78–2.00 Å. Analyzing the Nd–Al bonds formed after binding, it is evident that the bond distances are approximately 3.40 Å, while the Nd–O bond distances vary significantly from 2.45 to 2.64 Å. The binding energy values in Table 1 indicate that binding at the T1 site is slightly stronger (−2.38 eV) than at the T3 site (−2.33 eV), which is, in turn, stronger than at the T2 site (−1.92 eV).

The lowest-energy optimized structures for the binding of $[Yb(NO_3)_3(H_2O)_3]$ complexes at bulk-Tj BASs in the internal pore are shown in Fig. S1 (ESI†). In the bulk-T1-Yb structure, similar to bulk-T1-Nd, one of the H_2O molecules leaves the inner-coordination sphere but forms hydrogen bonds with the oxygen of –Al–O–Si– of the cluster and the bonded NO_3, with distances of 2.01 and 1.98 Å, respectively, resulting in an 8 coordinated complex. The optimization of the bulk-T2-Yb structure shows that it is a 9-coordinated complex, where all three attached H_2O

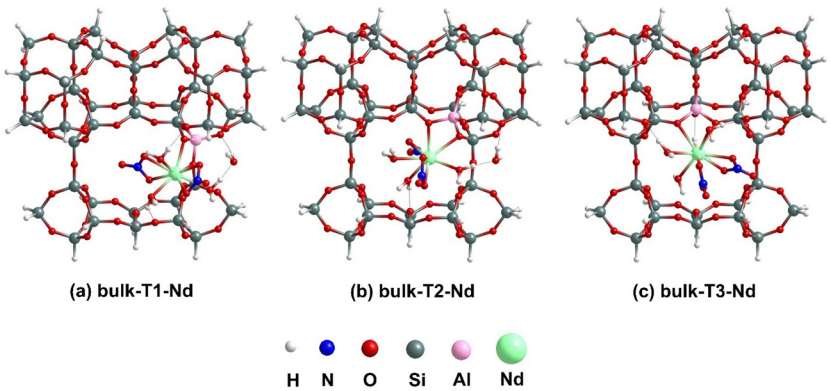

Fig. 3 Lowest energy optimized geometries for $[Nd(NO_3)_3(H_2O)_4]$ binding to T1, T2 and T3 BASs at internal pore using cluster models.

 This journal is © the Owner Societies 2025

Open Access Article. Published on 02 December 2024. Downloaded on 1/23/2026 9:32:19 PM.
This article is licensed under a Creative Commons Attribution-NonCommercial 3.0 Unported Licence.

Table 1 Binding energies, BE(BAS) (in eV), for $[X(NO_3)_3(H_2O)_n]$ at BASs at the internal pore

Model/analysis-internal pore BAS	Bulk-T1-X	Bulk-T2-X	Bulk-T3-X
Cluster/localized basis DFT X = Nd	−2.38	−1.92	−2.33
Cluster/localized basis DFT X = Yb	−2.32	−1.79	−2.07

Table 2 Comparison of binding energies, BE(BAS) (in eV), for $[X(NO_3)_3(H_2O)_n]$ (X = Nd, Yb) at bulk-T3 BAS at internal pore

Model/analysis-internal pore BAS	Bulk-T3-Nd	Bulk-T3-Yb
Cluster/localized basis DFT	−2.33	−2.07
Periodic/plane-wave DFT	−2.12	−1.76

molecules remain intact after binding, similar to the precursor $[Yb(NO_3)_3(H_2O)_3]$ complex. In the bulk-T3-Yb structure, the coordination environment around the Yb also remains 9 after binding, comprising two NO_3, three H_2O and two new bonds with the oxygens of –Al–O–Si– linkage of the cluster. For all three optimized bulk-Tj-Yb structures, two out of the three H_2O molecules attached to the Yb center interact with the oxygen of a –Si–O–Si– linkage of the cluster through hydrogen bonding interactions, with distances ranging from 1.74 to 1.99 Å. Yb being smaller in size, the Yb–Al bond lengths are approximately 3.20 Å, smaller than the Nd–Al bond lengths. Similar to Nd–O distances, the Yb–O distances also vary widely, from 2.31 to 2.45 Å. The binding energy strengths, as shown in Table 1, follow the trend: bulk-T1-Yb (−2.32 eV) > bulk-T3-Yb (−2.07 eV) > bulk-T2-Yb (−1.79 eV). Notably, the binding energy values for the bulk-Tj-Yb complexes are lower than those for the bulk-Tj-Nd complexes, indicating that Nd complexes bind more strongly at the internal pore of MCM-22 than Yb complexes.

3.2. Plane-wave DFT analysis

We further studied the binding of $[X(NO_3)_3(H_2O)_n]$ (X = Nd, Yb) at the bulk-T3 BAS in the internal pore employing plane-wave DFT calculations to provide further support for the validity of the results obtained from localized-basis calculations. Fig. 4(a) shows the configuration of $[Nd(NO_3)_3(H_2O)_4]$ binding at the bulk-T3 BAS site, while the $[Yb(NO_3)_3(H_2O)_3]$ binding configuration is shown in Fig. S2(a) in the ESI.† Similar to cluster calculations, the $[X(NO_3)_3(H_2O)_n]$ binding occurs through interactions between the X-center and Al, as well as various nearby O atoms in MCM-22. The Nd–Al and Yb–Al distances are calculated to be 3.44 and 3.22 Å, respectively, consistent with the cluster calculations. The variation in Nd–O (2.60–2.70 Å) and Yb–O (2.41–2.45 Å) distances is also evident from the plane-wave DFT calculations. Hydrogen bonding interactions between the attached H_2O molecules and oxygen of –Si–O–Si– linkage are 1.86–2.00 Å for Nd-bound cluster and 1.80–1.90 Å for Yb-bound cluster. Therefore, in terms of geometrical parameters, the localized-basis calculation aligns well with the plane-wave calculations. Table 2 compares the binding energies for $[X(NO_3)_3(H_2O)_n]$ binding at the bulk-T3 BAS using both cluster and periodic models. For the periodic model, the binding energy for $[Nd(NO_3)_3(H_2O)_4]$ binding at T3 site is −2.12 eV and for $[Yb(NO_3)_3(H_2O)_3]$ binding, it is −1.76 eV. The slight discrepancy between the binding energy results for the two methods is expected due to the different types of models employed for the MCM-22 material (periodic *vs.* cluster), and also the different functionals used in the DFT analysis. However, the stronger binding of $[Nd(NO_3)_3(H_2O)_4]$ to the BAS compared to $[Yb(NO_3)_3(H_2O)_3]$ is consistent in both calculations for the bulk-T3 BAS. It should be noted that, similar to our previous article,[23] the results from our cluster calculations align well with those from periodic calculations, where now we have incorporated explicit H_2O molecules in treating RE nitrate binding. This indicates that the results from our cluster calculations can be accurately translated to periodic calculations.

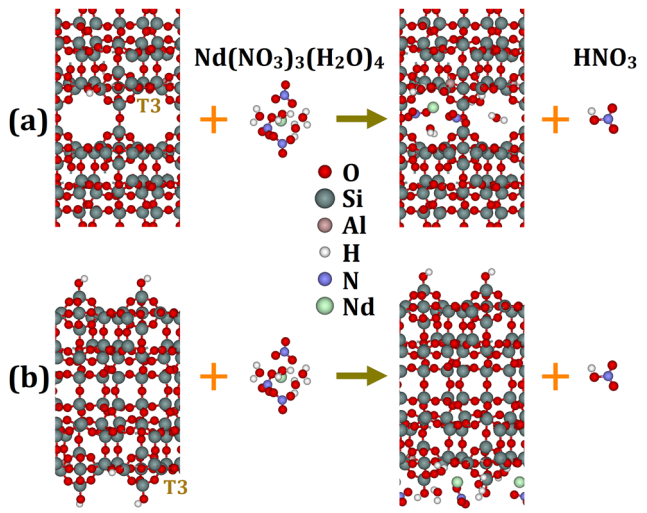

Fig. 4 Binding of $[Nd(NO_3)_3(H_2O)_4]$ complexes at BASs at (a) internal pore and (b) external surfaces of MCM-22. The overall reaction mechanism indicating all reactants and products is shown by using plus signs and arrows. All structures are optimized from our plane-wave DFT calculations. Nd nitrate binding reactions with an Al atom at the T3 site of the MCM-22 reactant.

4. RE nitrate binding at the external surface of MCM-22

4.1. Localized-basis DFT analysis

The lowest-energy optimized structures for the binding of $[Nd(NO_3)_3(H_2O)_4]$ complexes at a silanol site and at the surf-Tj BASs for the external surface cluster models are shown in Fig. 5. The coordination environment around the Nd center remains unchanged before and after binding for all three surface structures, maintaining a total CN of 10. For the surf-silanol-Nd, the Nd–Si distance is calculated to be 3.47 Å, whereas for surf-Tj–Nd, the Nd–Al distances are approximately 3.31 Å. The Nd–O distance in surf-silanol-Nd is 2.31 Å; however, the Nd–O distances for binding at BASs vary over a large range (2.53–2.64 Å) like the internal pore cluster models. The H_2O molecules coordinated to the Nd center are interacting with the cluster *via* the oxygen of a –Si–O–Si– linkage and an OH of a silanol group through hydrogen bonding interaction (1.75–1.99 Å). In addition,

Open Access Article. Published on 02 December 2024. Downloaded on 1/23/2026 9:32:19 PM.
This article is licensed under a Creative Commons Attribution-NonCommercial 3.0 Unported Licence.

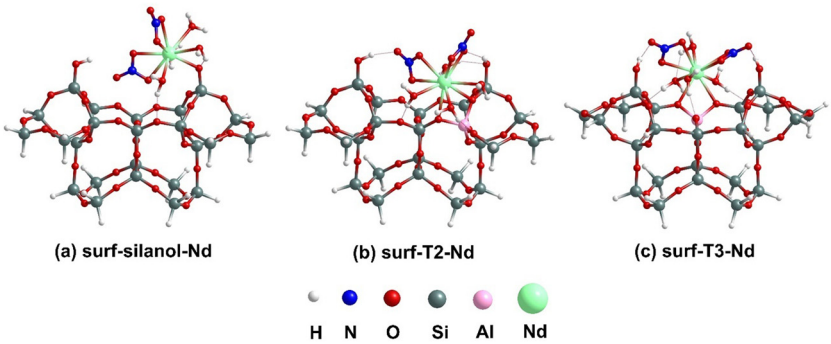

Fig. 5 Lowest energy optimized geometries for $[Nd(NO_3)_3(H_2O)_4]$ binding to silanol site and T2, and T3 BASs at external surface using cluster models.

the bound nitrates also interact with the Si–OH moiety of the cluster through their oxygen ends *via* hydrogen bonding of distances 1.76–1.90 Å. In terms of binding energy, the surf-silanol-Nd structure experiences the lowest binding energy (−0.26 eV) compared to the surf-Tj-Nd even after considering explicit water molecules to satisfy the coordination environment of Nd. Analogous to our previous analysis without explicit H_2O,[23] the surf-T3-Nd has a stronger binding (−2.23 eV) than surf-T2-Nd (−2.04 eV). Therefore, it is apparent that regardless of the coordination environment around Nd center, Nd complexes bind more strongly to BASs compared to silanol sites.

The lowest-energy optimized geometries for the binding of $[Yb(NO_3)_3(H_2O)_3]$ complexes at the silanol site and surf-Tj BASs on the external surface are shown in Fig. S3 (ESI†). Similar to the Nd-bound surface cluster, the coordination number around the Yb center remains unchanged before and after binding, maintaining it at 9. The Yb–Si distance for surf-silanol-Yb is 3.24 Å, which is 0.06 Å longer than the Yb–Al distances (∼3.18 Å) for surf-Tj-Yb. The Yb–O distance for surf-silanol-Yb is 2.17 Å, while it varies between 2.37 and 2.42 Å for surf-Tj-Yb. The interaction between the coordinated H_2O molecules and the cluster is evident from the hydrogen bonding between the oxygen of the –Si–O–Si– linkage and the OH of the silanol group (1.69–1.83 Å). Additionally, the nitrates attached to the Yb center interact with the cluster *via* the silanol group, forming O···HO hydrogen bonds with distances ranging from 1.86 to 1.93 Å. Here also, the surf-silanol-Yb has the lowest binding energy (−0.54 eV) among all Yb-bound surface geometries. Interestingly, unlike Nd-bound surface complexes, here the binding at surf-T2 site (−2.29 eV) is stronger than surf-T3 site (−2.19 eV) by ∼0.10 eV. Moreover, the binding at surf-T2 is energetically comparable with bulk-T1, suggesting that for Yb complexes, both bulk-T1 and surf-T2 sites are equally competitive. Notably, when comparing the binding of Nd and Yb complexes at the external surface, it is evident that Yb experiences stronger binding at the external surface than Nd (Table 3).

4.2. Plane-wave DFT analysis

For the external surface, we also studied the binding of $[X(NO_3)_3(H_2O)_n]$ (X = Nd, Yb) at the surf-T3 BAS using plane-wave DFT calculations to compare the results from the two DFT methods. Fig. 4(b) shows the configuration of $[Nd(NO_3)_3(H_2O)_4]$ binding at the surf-T3 BAS site, while $[Yb(NO_3)_3(H_2O)_3]$ binding is given in Fig. S2(b) in the ESI.† Similar to the cluster models, the binding at the external BAS occurs through the interaction of the X-center with Al and nearby O atoms. The calculated Nd–Al and Yb–Al distances are 3.37 Å and 3.24 Å, respectively, which are consistent with the cluster calculations. The variation in Nd–O (2.58–2.60 Å) and Yb–O (2.41 Å) distances is also in a similar range to that observed in the localized-basis calculations. Additionally, the hydrogen bonding interactions between the attached H_2O molecules and oxygen of –Si–O–Si– linkage and the silanol group are also found in a similar range. Therefore, in terms of geometrical parameters, the structures optimized using localized-basis calculation are comparable to that of plane-wave DFT calculations. Table 4 compares the binding energies for $[X(NO_3)_3(H_2O)_n]$ binding at the surf-T3 BAS using both cluster and periodic models. The binding energy for $[Nd(NO_3)_3(H_2O)_4]$ binding at surf-T3 is −2.01 eV, and for $[Yb(NO_3)_3(H_2O)_3]$ binding, it is −1.61 eV using plane-wave DFT calculations. Again, a discrepancy in binding energy between the two methods occurs because of the adoption of two different models for the MCM-22 material (periodic *vs.* cluster) and the use of two different DFT functionals for the calculations. The plane-wave DFT shows a larger difference between the Nd and Yb binding energies than the localized basis cluster models. However, the trends are similar. Therefore, for surface calculations, the results for Nd complex binding show reasonable agreement between our cluster and periodic calculations, but for Yb complex binding, there is some discrepancy in the binding energy value between the two methods.

Table 3 Binding energies, BE(silanol) and BE(BAS) (in eV), for $[X(NO_3)_3(H_2O)_n]$ at silanol and BASs at external surface

Model/analysis-external silanol/BAS	Surf-silanol-X	Surf-T2-X	Surf-T3-X
Cluster/localized basis DFT X = Nd	−0.26	−2.04	−2.23
Cluster/localized basis DFT X = Yb	−0.54	−2.29	−2.19

Table 4 Comparison of binding energies, BE(BAS) (in eV), for $[X(NO_3)_3(H_2O)_n]$ (X = Nd, Yb) at surf-T3 BAS at external surface

Model/analysis-external surface BAS	Surf-T3-Nd	Surf-T3-Yb
Cluster/localized basis DFT	−2.23	−2.19
Periodic/plane-wave DFT	−2.01	−1.61

This journal is © the Owner Societies 2025

Open Access Article. Published on 02 December 2024. Downloaded on 1/23/2026 9:32:19 PM. This article is licensed under a Creative Commons Attribution-NonCommercial 3.0 Unported Licence.

5. Discussion and conclusion

We have performed a comprehensive DFT analysis of the binding of RE nitrate aqua complexes, $[X(NO_3)_3(H_2O)_n]$ (X = Nd, Yb) to MCM-22. This study primarily utilized localized-basis DFT calculations with cluster models, but we further validated our results using plane-wave DFT calculations with periodic models for a few selected binding configurations. The energetics obtained from the plane-wave DFT calculations align well with those from localized-basis calculations in most cases. This consistency suggests that our cluster models are adequate representations of the periodic MCM-22 models for binding studies. For both RE nitrate aqua complexes, as observed in our previous article,[23] the binding at BASs is significantly stronger than at silanol sites, aligning with the observed trend of increased RE adsorption with higher Al content.[16]

Considering cluster models, for Nd-complexes, the maximum binding strength at BASs in the internal pore (at bulk-T1) is around −2.38 eV, which is slightly stronger than the maximum binding strength at BASs on the external surface (at surf-T3, −2.23 eV). Thus Nd-complexes exhibit a slight preference to adsorb within the internal pores (although this could be countered by transport limitations). In the case of Yb-complexes, the localized-basis calculations show that the binding strength is comparable at both bulk-T3 BAS in the internal pore (−2.32 eV) and surf-T2 BAS on the external surface (−2.29 eV), *i.e.*, there is a comparable preference for binding at internal pores and external surfaces of MCM-22. To investigate the reason behind the difference in behavior for Nd *versus* Yb, we have performed a geometrical parameter analysis, provided in Table S1 (ESI†). It shows that for bulk-T1-Nd and surf-T3-Nd structures, the Nd–Al distances are relatively consistent in both the structures. However, the Nd–O distances are quite different; 2.45 and 2.61 Å in bulk-T1-Nd structure and 2.53 and 2.55 Å in surf-T3-Nd structure. So, in the former case, one of the Nd-O distances is longer, whereas for the later both the Nd–O distances are quite long. These longer Nd–O distances in the surface structure correspond to weaker interactions, which might be the reason behind the lower binding strength of Nd complexes on the external surface compared to the internal pore. In contrast, for Yb complexes, both the Yb–Al and Yb–O distances remain comparable in the internal pore and on the external surface. This similarity in bond distances might account for the similar binding strengths observed for Yb complexes in both the internal pore and external surface.

Another noticeable observation is that the binding of Nd complexes at the internal pore is stronger than Yb complexes, whereas comparable binding strengths or the reverse trend applies on the external surface. This different trend cannot be explained by any single factor as several factors, such as structural difference between Nd and Yb complexes, including the number of coordinated H_2O molecules, the accommodation of these complexes within internal pores or on external surfaces, hydrogen bonding between coordinated H_2O molecules and the cluster, and the orientation of nitrate and H_2O molecules post-optimization influence the binding and so the binding energy.

A comparison between $X(NO_3)_3$[23] binding and $[X(NO_3)_3(H_2O)_n]$ binding shows that the binding energy values increase in the presence of explicit H_2O. This enhancement can be attributed to the formation of hydrogen bonding interactions between the bound H_2O molecules and MCM-22. See Table 5 which compares behavior for $Nd(NO_3)_3$ and $[Nd(NO_3)_3(H_2O)_4]$ from the cluster model, and see the ESI† for additional results. On the other hand, trends of binding energies, *e.g.*, comparing different binding sites, remain substantially the same, *i.e.*, saturating the coordination environment around the RE cations does not affect such trends. However, the binding scenario can be more complicated for the RE nitrate aqua complex, *e.g.*, as reflected in a change in CN due to the loss of a water molecule from the first coordination sphere for binding at the internal pore, but not at the external surface.

Overall, our modeling approach provides a realistic representation of the binding of RE nitrates on MCM-22 clay mimics. This comprehensive analysis provides valuable insights into the binding mechanisms of RE complexes on MCM-22, a topic that has been relatively underexplored until now.

Data availability

The data supporting this article have been included as part of the ESI.†

Conflicts of interest

The authors declare no conflicts of interest.

Acknowledgements

This work was supported by the U.S. Department of Energy (DOE), Office of Science, Basic Energy Sciences, Chemical Sciences, Geosciences, and Biosciences Division. TA & YH were supported by the Geo-inspired Separation of Rare-earth Elements project, and JWE & TLW by the Computational & Theoretical Chemistry project. The research was performed at Ames National Laboratory, which is operated by Iowa State University under contract No. DE-AC0207CH11358. DFT calculations were performed with a grant of computer time at the National Energy Research Scientific Computing Center (NERSC). NERSC is a DOE Office of Science User Facility supported by the

Table 5 Comparison of binding energies (in eV) for $Nd(NO_3)_3$ and $[Nd(NO_3)_3(H_2O)_4]$ from cluster model calculations

Internal pore $Nd(NO_3)_3$	−1.97 (T1)	−1.69 (T2)	−1.75 (T3)
Internal pore $[Nd(NO_3)_3(H_2O)_4]$	−2.38 (T1)	−1.92 (T2)	−2.33 (T3)
External surface $Nd(NO_3)_3$	−0.19 (silanol)	−1.33 (T2)	−1.59 (T3)
External surface $[Nd(NO_3)_3(H_2O)_4]$	−0.26 (silanol)	−2.04 (T2)	−2.23 (T3)

Office of Science of the U.S. DOE under Contract No. DE-AC02-05CH11231.

Open Access Article. Published on 02 December 2024. Downloaded on 1/23/2026 9:32:19 PM. This article is licensed under a Creative Commons Attribution-NonCommercial 3.0 Unported Licence.

References

1 E. Alonso, A. M. Sherman, T. J. Wallington, M. P. Everson, F. R. Field, R. Roth and R. E. Kirchain, *Environ. Sci. Technol.*, 2012, **46**, 3406–3414.
2 S. Massari and M. Ruberti, *Resour. Policy*, 2013, **38**, 36–43.
3 M. A. de Boer and K. Lammertsma, *ChemSusChem*, 2013, **6**, 2045–2055.
4 P. Ascenzi, M. Bettinelli, A. Boffi, M. Botta, G. De Simone, C. Luchinat, E. Marengo, H. Mei and S. Aime, *Rend. Sedute Accad. Naz. Lincei, Cl. Sci. Fis., Mat. Nat.*, 2020, **31**, 821–833.
5 T. I. Kostelnik and C. Orvig, *Chem. Rev.*, 2019, **119**, 902–956.
6 C. Bouzigues, T. Gacoin and A. Alexandrou, *ACS Nano*, 2011, **5**, 8488–8505.
7 J. Wang and S. Li, *Front. Med.*, 2022, **9**, 946100.
8 Z. Wei, Y. Liu, B. Li, J. Li, S. Lu, X. Xing, K. Liu, F. Wang and H. Zhang, *Light: Sci. Appl.*, 2022, **11**, 175.
9 P. C. Dent, *J. Appl. Phys.*, 2012, **111**, 07A721.
10 J. M. D. Coey, *Engineering*, 2020, **6**, 119–131.
11 J. Guo, S. Chen, W. Chen, X. Huang and T. Cui, *Front. Electron. Mater.*, 2022, **2**, 906213.
12 X. Zhong, Y. Sun, T. Iitaka, M. Xu, H. Liu, R. J. Hemley, C. Chen and Y. Ma, *J. Am. Chem. Soc.*, 2022, **144**, 13394–13400.
13 X. Feng, O. Onel, M. Council-Troche, A. Noble, R.-H. Yoon and J. R. Morris, *Appl. Clay Sci.*, 2021, **201**, 105920.
14 S. Qiu, T. Qiu, H. Yan, Q. Long, H. Wu, X. Li and D. Zhu, *Colloids Surf., A*, 2022, **642**, 128596.
15 A. M. Borst, M. P. Smith and A. A. Finch, *et al.*, *Nat. Commun.*, 2020, **11**, 4386.
16 P. Chatterjee, Y. Han, T. Kobayashi, K. K. Verma, M. Mais, R. K. Behera, T. H. Johnson, T. Prozorov, J. W. Evans and I. I. Slowing, *et al.*, *ACS Appl. Mater. Interfaces*, 2023, **15**, 54192–54201.
17 G. G. Juttu and R. F. Lobo, *Microporous Mesoporous Mater.*, 2000, **40**, 9–23.
18 W. J. Roth and D. L. Dorset, *Microporous Mesoporous Mater.*, 2011, **142**, 32–36.
19 W. J. Roth, J. Čejka, R. Millini, E. Montanari, B. Gil and M. Kubu, *Chem. Mater.*, 2015, **27**, 4620–4629.
20 K. Okumura, M. Hashimoto, T. Mimura and M. Niwa, *J. Catal.*, 2002, **206**, 23–28.
21 A. Corma, U. Díaz, T. García, G. Sastre and A. Velty, *J. Am. Chem. Soc.*, 2010, **132**, 15011–15021.
22 Y. Han, P. Chatterjee, S. B. Alam, T. Prozorov, I. I. Slowing and J. W. Evans, *Phys. Chem. Chem. Phys.*, 2023, **25**, 4680–4689.
23 Y. Han, T. Ash, P. Chatterjee, W. Huang, T. L. Windus and J. W. Evans, *J. Phys. Chem. C*, 2024, **128**, 6309–6318.
24 M. E. Leonowicz, J. A. Lawton, S. L. Lawton and M. K. Rubin, *Science*, 1994, **264**, 1910–1913.
25 G. Sastre, V. Fornes and A. Corma, *J. Phys. Chem. B*, 2000, **104**, 4349–4354.
26 D. Zhou, Y. Bao, M. Yang, N. He and G. Yang, *J. Mol. Catal. A: Chem.*, 2006, **244**, 11–19.
27 Y. Li, W. Guo, W. Fan, S. Yuan, J. Li, J. Wang, H. Jiao and T. Tatsumi, *J. Mol. Catal. A: Chem.*, 2011, **338**, 24–32.
28 Y. Wang, D. Zhou, G. Yang, S. Miao, X. Liu and X. Bao, *J. Phys. Chem. A*, 2004, **108**, 6730–6734.
29 D. J. Rogers, N. J. Taylor and G. E. Toogood, *Acta Crystallogr.*, 1983, **39**, 939–941.
30 *National Center for Biotechnology Information, PubChem Compound Summary for CID 16211525, Ytterbium(III) nitrate pentahydrate*, *PubChem*, 2024, **https://pubchem.ncbi.nlm.nih.gov/compound/Ytterbium_III_-nitrate-pentahydrate**.
31 A. Zheng, L. Chen, J. Yang, M. Zhang, Y. Su, Y. Yue, C. Ye and F. Deng, *J. Phys. Chem. B*, 2005, **109**, 24273–24279.
32 S. Wang, Z. Wei, Y. Chen, Z. Qin, H. Ma, M. Dong, W. Fan and J. Wang, *ACS Catal.*, 2015, **5**, 1131–1144.
33 E. Aprà, E. J. Bylaska, W. A. de Jong, N. Govind, K. Kowalski, T. P. Straatsma, M. Valiev, H. J. Van Dam, Y. Alexeev and J. Anchell, *et al.*, *J. Chem. Phys.*, 2020, **152**, 184102.
34 J. P. Perdew, M. Ernzerhof and K. Burke, *J. Chem. Phys.*, 1996, **105**, 9982–9985.
35 C. Adamo and V. Barone, *J. Chem. Phys.*, 1999, **110**, 6158–6170.
36 F. Weigend and R. Ahlrichs, *Phys. Chem. Chem. Phys.*, 2005, **7**, 3297–3305.
37 F. Weigend, *Phys. Chem. Chem. Phys.*, 2006, **8**, 1057–1065.
38 B. P. Pritchard, D. Altarawy, B. Didier, T. D. Gibson and T. L. Windus, *J. Chem. Inf. Model.*, 2019, **59**, 4814–4820.
39 K. L. Schuchardt, B. T. Didier, T. Elsethagen, L. Sun, V. Gurumoorthi, J. Chase, J. Li and T. L. Windus, *J. Chem. Inf. Model.*, 2007, **47**, 1045–1052.
40 S. Grimme, J. Antony, S. Ehrlich and H. Krieg, *J. Chem. Phys.*, 2010, **132**, 154104.
41 G. Kresse and J. Furthmüller, *Phys. Rev. B: Condens. Matter Mater. Phys.*, 1996, **54**, 11169–11186.
42 G. Kresse and D. Joubert, *Phys. Rev. B: Condens. Matter Mater. Phys.*, 1999, **59**, 1758–1775.
43 J. Klimeš, D. R. Bowler and A. Michaelides, *J. Phys.: Condens. Matter*, 2010, **22**, 022201.
44 Y. Han, K. C. Lai, A. Lii-Rosales, M. C. Tringides, J. W. Evans and P. A. Thiel, *Surf. Sci.*, 2019, **685**, 48–58.
45 Y. Han, M. C. Tringides, J. W. Evans and P. A. Thiel, *Phys. Rev. Res.*, 2020, **2**, 013182.
46 Y. Han, J. W. Evans and M. C. Tringides, *Appl. Phys. Lett.*, 2021, **119**, 033101.
47 X. Wang and Y. Han, *Comput. Mater. Sci.*, 2023, **224**, 112153.
48 Y. Han, M. Kolmer, M. C. Tringides and J. W. Evans, *Carbon*, 2023, **205**, 336–344.
49 Y. Han, *AIP Adv.*, 2022, **12**, 125009.
50 Y. Han, P. Chatterjee, S. B. Alam, T. Prozorov, I. I. Slowing and J. W. Evans, *Phys. Chem. Chem. Phys.*, 2023, **25**, 4680–4689.

 This journal is © the Owner Societies 2025